

# A CMOS Energy Harvesting Interface Circuit With Cycle-to-Cycle Frequency-to-Amplitude Conversion MPPT for Centimeter-Scale Wind Turbine

Zizhen Zeng<sup>ID</sup>, Student Member, IEEE, Johan J. Estrada-López<sup>ID</sup>, Member, IEEE,  
Bo Wang<sup>ID</sup>, Member, IEEE, and Edgar Sánchez-Sinencio<sup>ID</sup>, Life Fellow, IEEE

**Abstract**—An energy harvesting (EH) system is proposed to extract energy from a centimeter-scale electromagnetic (EM) micro wind turbine. To improve the end-to-end efficiency, an autonomous and self-biased active rectifier is employed. A hysteresis-controlled boost converter is designed with self-zero-current-switching calibrations, which achieves a peak DC-DC efficiency of 93.3% with a maximum efficiency improvement of 12.7%. In addition, a novel frequency-to-amplitude conversion (FAC) maximum power point tracking (MPPT) method is proposed for a cycle-to-cycle MPPT. In measurements, the proposed FAC MPPT requires no more than three cycles to locate the maximum power point (MPP) in abrupt frequency changes, with an 80% tracking accuracy in the first turbine cycle. In wind-field testing, the EH system starts to track the MPP one cycle after start-up at 2.0 V. In the steady-state, the EH system maintains its cycle-to-cycle MPP under different wind conditions. In wind-field testing for wind speeds from 1.0 to 5.0 m/s, the peak MPPT accuracy is 99.27%, with an MPPT efficiency of 99.85%. The extracted power is from 0.1 to 8 mW with a peak end-to-end efficiency of 88.2%. Compared to a full-bridge rectifier, a 630% energy extraction gain is measured at a low wind speed of 1.2 m/s. To the best of the authors' knowledge, this is the first IC prototype for a cm-scale EM wind turbine EH to achieve a cycle-to-cycle MPPT with the highest reported MPPT efficiency.

**Index Terms**—cm-scale, electromagnetic, energy harvesting, frequency-to-voltage converter, maximum power point tracking, micro wind turbine, rectifier, zero-current-switching.

## I. INTRODUCTION

AMBIENT wind is a free, abundant, and promising energy source to enable the Internet-of-Things (IoT) edge-sensing applications in remote outdoor areas [1]–[3],

Manuscript received December 2, 2020; revised March 20, 2021 and June 5, 2021; accepted June 6, 2021. This work was supported in part by Texas Instruments, in part by Silicon Labs, in part by Qualcomm, and in part by NPRP through the Qatar National Research Fund (a member of Qatar Foundation) under Grant NPRP11S-0104-180192. This article was recommended by Associate Editor M. Hella. (Corresponding author: Zizhen Zeng.)

Zizhen Zeng is with the Department of Electrical and Computer Engineering, Texas A&M University, College Station, TX 77843 USA (e-mail: zzzeng@tamu.edu).

Johan J. Estrada-López is with the Faculty of Mathematics, Autonomous University of Yucatán, Mérida 97000, Mexico.

Bo Wang is with the Division of Information and Computing Technology, College of Science and Engineering, Hamad Bin Khalifa University, Doha, Qatar.

Edgar Sánchez-Sinencio, deceased, was with the Department of Electrical and Computer Engineering, Texas A&M University, College Station, TX 77843 USA (e-mail: s-sanchez@tamu.edu).

Color versions of one or more figures in this article are available at <https://doi.org/10.1109/TCSI.2021.3087790>.

Digital Object Identifier 10.1109/TCSI.2021.3087790

or in indoor ventilating systems [4], [5]. For these IoT applications, the form factor of the harvester is preferred to be minimized while its harvested power, especially at low wind speed, is desired to be maximized. Robustness and reliability of the harvester are also of special concern. Therefore, research on micro-scale energy harvesters for low-wind-speed is gaining a lot of attention [6]–[8]. To minimize the harvester volume and to operate at the minimum wind speed, micro-mechanical structures are proposed [9], and piezoelectric materials are explored [10]. Among various types of wind energy harvesters, the rotary electromagnetic (EM) wind turbine generator (WTG) has proved to be a reliable solution because of its relatively small size, low-cost, compatible voltage levels, and considerable output power at low-wind-speed conditions [2], [3]. The moderate output voltage (1-3 V) and sufficient power ( $\mu$ W-mW) of centimeter-scale WTGs are also suitable for standard CMOS technologies, which can provide a low-cost solution for many low-power IoT applications [2]–[5], [11]–[14]. However, the wind power profile can be very sparse under different weather conditions, which requires the system to have self-start-up and autonomous operation abilities, especially when the wind is weak or even absent. Meanwhile, the incoming wind is difficult to predict, and its speed can change drastically in a very short period [1]. Therefore, a power-efficient EH system is demanded to extract the most available energy under different wind conditions and extend its operation range close to the minimum cut-in wind speed.

To ensure maximum power extraction under such conditions, a maximum power point tracking (MPPT) method is required to optimize the overall system's performance. However, most of the existing MPPT solutions for large-scale wind EH systems are not applicable for ultra-low-power IoT applications because they require complex algorithms or expensive computation elements [15]–[17]. The conventional open-circuit voltage  $V_{OC}$  detection method commonly used in low-power MPPT is also not adequate for fast-tracking required by the frequently-changing wind conditions [18]. Illustrated in [4], the conventional  $V_{OC}$ -based MPPT cannot detect the actual wind speed variance, which leads to zero energy efficiency in the worst case even with 100% MPPT power efficiency. Therefore, an algorithm with the adaptive sampling rate is proposed in [4] to harvest the predictable wind energy from the passing trains. However, this scheme requires an accurate prediction on wind power, which is extremely difficult to achieve for the ambient wind EH.

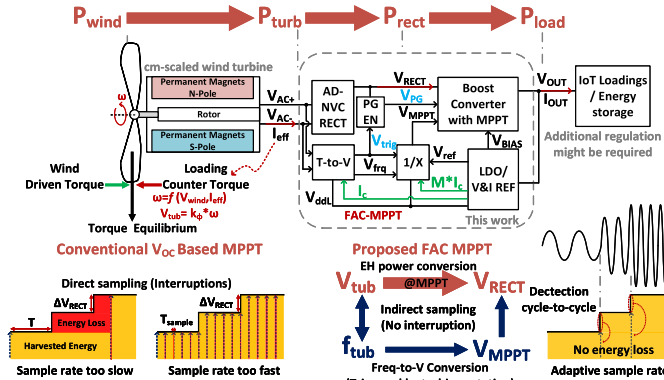


Fig. 1. Proposed wind energy harvester system with FAC MPPT.

Moreover,  $V_{oc}$  detection interrupts the energy transfer, changes the loading condition of the EH source, and degrades the system reliability with high voltage stress [19]. To provide other feasible low-cost solutions for MPPT, an auxiliary generator is used to replicate the open-circuit voltage in [20]. The internal resistance or inductance values have been examined in [3], [21], [22]. However, those techniques require an accurate model of the target EH source, which is not available for many low-profile wind turbines. Moreover, the constant-parameter approximation is not valid for wide-range operations. Additionally, the power consumption is relatively high compared to the deliverable power because the voltage or current information must be monitored continuously or relies on high switching-frequency operations [11], [22]. A conduction-angle-based low-power MPPT is proposed to update by cycles [19], but its trade-off between the response time and step resolution makes it unsuitable for fast-tracking applications. Therefore, a low-cost, low-power, and fast response method is desired to ensure a cycle-to-cycle MPPT for wind energy harvesting.

Fig. 1 shows the proposed wind energy harvesting system. The permanent magnet generator driven by the blade converts the mechanical power into electrical power. For the AC-DC power conversion, the conventional full-bridge rectifier will introduce a considerable forward-voltage loss. Therefore, an active-diode embedded negative voltage converter (AD-NVC) with a self-biased comparator is proposed in this work to improve the power conversion efficiency, especially in low-voltage domains. Also shown in Fig. 1, the  $V_{oc}$ -based MPPT with fixed and free-running sampling rate suffers from considerable energy loss when the available energy is changed. Conceptually, the maximum power point (MPP) only needs to be updated when the input power is changed. And the energy in a wind turbine is reflected by cycles [2]. Therefore, an MPPT algorithm which can detect the changes of incoming wind speed from cycle to cycle ensures overall high energy efficiency. Without using an auxiliary wind turbine or wind speed sensors, this work utilizes the linear relationship between the motor rotation frequency and its induced AC voltage amplitude [2]. A novel frequency-to-amplitude conversion (FAC) MPPT is proposed to monitor the turbine rotation frequency that determines the MPPT voltage. The proposed FAC MPPT solution has no interruptions on energy transfer because the wind turbine also serves as a wind

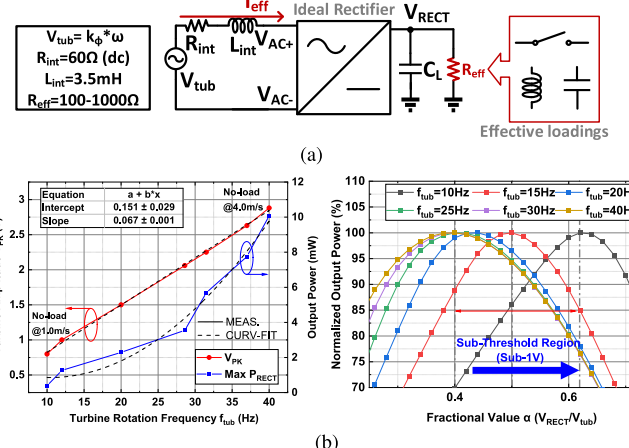


Fig. 2. (a) Wind turbine electrical model and (b) electrical characteristics without considering loading effects, AD-NVC is adopted.

power sensor simultaneously. After the rectifier, a DC-DC boost converter performs the MPPT operation to maximize the power extraction and boost up the output voltage for energy storage. The loading can be a specific circuit load for IoT edge-sensing applications or a capacitor buffer for temporal energy storage. Additionally, a low-dropout regulator (LDO) is implemented to provide a stable supply and a reference voltage for the FAC MPPT. This paper is structured as follows. Section II will discuss the details of circuit implementation and analysis. Section III provides measurement results and compares them with previous designs. Finally, Section IV will offer a summary of this work.

## II. SYSTEM IMPLEMENTATION AND ANALYSIS

To build a power-efficient system for wind EH, the system optimization for the target input voltage and input power is significant. Also, the EH system is designed for autonomous and asynchronous operations to accommodate unpredictable wind behaviors. In this section, the centimeter-scale WTG's electrical characteristics are first examined with an analysis of MPPT operations. Then, the circuit blocks in the proposed EH system are introduced individually.

### A. Turbine Electrical Model and Its Maximum Power Point

Although mini wind ad-hoc harvesters can be designed [14], a low-cost WTG can be implemented by adapting either an airscrew [2] or Savonius [12] propeller to a commercial electromagnetic generator. Fig. 2a is the first-order electrical model of the adopted WTG for maximum power point analysis. The internal resistor  $R_{int}$  and inductor  $L_{int}$  represent the winding wire and the internal loss, respectively [2].  $R_{int}$  is 60  $\Omega$  at DC and  $L_{int}$  is 3.5 mH. Since the reactance is less than 1% compared to the resistance, the effective resistive loading  $R_{eff}$  only needs to be matched with  $R_{int}$  for ideal maximum power extraction. From load-pull measurements,  $R_{eff}$  ranges from 100 to 1000  $\Omega$ , and  $R_{int}$  equals 100  $\Omega$  through a curve-fitting approach.

Fig. 2b shows the turbine output amplitude  $V_{pk}$  at different rotation frequencies. The corresponding wind speed is covered from 1.0 to 4.0 m/s (WTG rotation frequency  $f_{tub}$  from 10 to 40 Hz). Theoretically, the amplitude of the WTG's

output  $V_{\text{tub}}$  depends on  $f_{\text{tub}}$ , which is also shown in Fig. 2b. The angular rotation speed of the WTG's rotor under different loading conditions is determined by [1]:

$$\omega = v \times \frac{\lambda}{R} - k \times I_{\text{eff}} \quad (1)$$

In (1),  $v$  is the coming wind speed;  $\lambda$  is the coefficient between wind speed and rotor frequency, and it is constant if the wind blade attack angle is fixed without gear control [2];  $R$  is the outer blade radius. Therefore, the angular rotation speed  $\omega$  is linearly proportional to the wind speed based on the blade aerodynamics structure. However, when loaded by a current  $I_{\text{eff}}$ , a counter torque is generated to resist the wind-driven torque, and  $\omega$  is decreased by this loading effect factor  $k$  [1], [2]. The final  $\omega$  is balanced under the torque equilibrium effect, and this effect performs as an additional loss, which is inevitable in WTG, and is expressed as the Betz limit (59.3%). Even so,  $V_{\text{tub}}$  is still given by:

$$V_{\text{tub}} = k_{\phi} \times \omega \quad (2)$$

In (2),  $k_{\phi}$  is the magnetic field constant provided by permanent magnets [3]. Therefore, the induced voltage  $V_{\text{tub}}$  amplitude is proportional to  $\omega$  under different loading conditions. When  $R_{\text{eff}}$  equals  $R_{\text{int}}$ , the output power  $P_{\text{RECT}}$  achieves its maximum value as:

$$P_{\text{RECT}_{\text{MAX}}} = \frac{V_{\text{tub}}^2}{8 \times R_{\text{int}}}, \text{ where } V_{\text{RECT}} = \alpha \times V_{\text{tub}} \quad (3)$$

In (3), the fractional value  $\alpha$  is the ratio between  $V_{\text{RECT}}$  and  $V_{\text{tub}}$ , which typically ranges from 0.4–0.6 [18], [23]. And  $V_{\text{AC}}$  under open-circuit conditions is commonly adopted since  $V_{\text{tub}}$  is not accessible directly. And in our proposed FAC MPPT algorithm,  $V_{\text{tub}}$  is converted by detected  $f_{\text{tub}}$  with prerequisite  $k_{\phi}$  or by measurement results (Fig. 2b).

In Fig. 2b, the normalized extracted output power in simulations is also plotted with the actual rectifier. The optimal  $\alpha$  is from 0.6 to 0.4, depending on the operation range. In the low  $f_{\text{tub}}$  range,  $\alpha$  is close to 0.6, which is also affected by sub-threshold operations of the rectifier. When  $V_{\text{tub}}$  is smaller than 1 V, the loading voltage (0.4–0.6 V) is comparable with the device threshold voltage (0.5 V), a higher loading voltage (larger  $\alpha$ ) in this case can reduce the conduction loss and ensure the AD-NVC operation. For higher  $f_{\text{tub}}$  (larger  $V_{\text{tub}}$ ), the optimal  $\alpha$  is close to 0.4 with adequate voltage headroom. As a compromise, an  $\alpha$  at 0.5 still ensures an 85% to 95% extraction efficiency for the whole range.

In Fig. 3a and Fig. 3b, the loading effect in PRECT and optimal  $\alpha_{\text{OC}}$  ( $V_{\text{tub}}$  is replaced by  $V_{\text{OC}}$ ) is simulated. To avoid parameter iterations, a first-order approximation is used by setting  $I_{\text{eff}}$  equal to the RMS value of  $V_{\text{tub}}/(R_{\text{int}} + R_{\text{eff}})$ . Even so, the loading effects are well illustrated with different loading effect factor  $k$ . With increasing  $k$ , the generated output power is decreased and the optimal  $\alpha_{\text{OC}}$  is also shifted to a higher value. The loading effect degrades the MPPT efficiency and accuracy, especially in conventional MPPT methods which evaluate the AC amplitude in the open-circuit condition. However, in our proposed FAC MPPT, the actual  $V_{\text{tub}}$  is derived from the detected  $f_{\text{tub}}$ , which decouples the loading effect (by (2)). Up to now, the loading

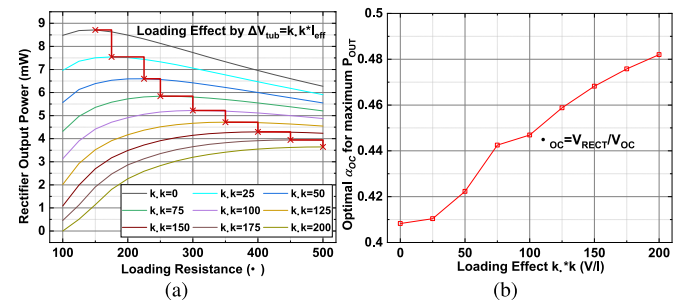
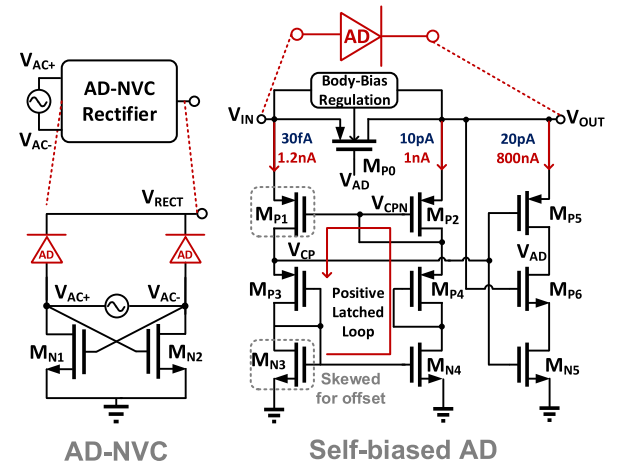


Fig. 3. Loading effects in (a) PRECT degradation and (b) optimal  $\alpha$  shift.



AD-NVC      Self-biased AD

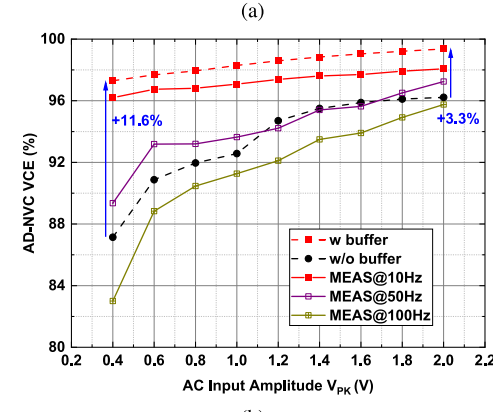


Fig. 4. (a) AD-NVC rectifier and (b) VCE performance comparison.

effect and the optimal  $\alpha$  selection for wide range operations have been discussed. Furthermore, to minimize the potential performance degradation,  $\alpha$  should be programmable to determine the optimal value in field-testing.

#### B. AC-DC NVC Rectifier and Active Diode Design

To achieve autonomous operations and self-start-up, conventional active rectifiers are not suitable because they need additional control circuits and well-start-up power supplies. Fig. 4a shows the AD embedded NVC (AD-NVC) rectifier architecture details. The PMOS pair is controlled by the AD comparator to reduce the reversed leakage current in conventional NVCs [24]–[26]. Compared to two-step conversion with an additional AD [24], [25], the AD-NVC [26], [27] only has four conduction transistors. Its area is reduced

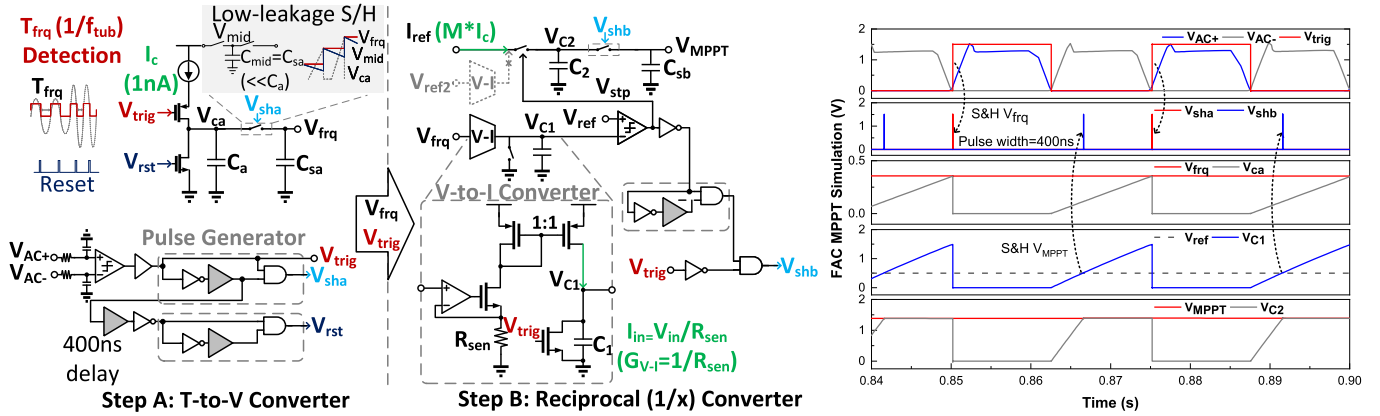


Fig. 5. Frequency-to-Amplitude conversion MPPT schematic and its simulation waveform.

by 20% since the size of the conduction transistor is dominant ( $6\times$  larger than the comparator). To ensure the system's self-start-up and autonomous operation, a self-biased current-mode comparator with a positive latched feedback loop [28] is adopted. Stack of devices ( $M_{P3,4}$ ) are added to minimize the biasing current and adjust the latched loop response. Additionally, a short-through current suppression buffer (by  $M_{P5}$ ,  $M_{P6}$ , and  $M_{N5}$ ) is added to provide the rail-to-rail control voltage  $V_{AD}$ . The diode-connected  $M_{P6}$  serves as a current limiter. Meanwhile,  $M_{P5}$  and  $M_{N5}$  are sized to have different flip-point values. The typical idle current is 30 pA when the input signal is absent (When  $V_{IN} = 0$ , the right branches are also disabled with the AD to cut off the reverse leakage). And the average current in active mode is 800 nA, without any additional control circuits or additional start-up mechanism [29], which can handle the sparse wind power while providing high power conversion efficiency. Additionally, bulk regulation is added by a cross-coupled PMOS selector. The offset is also skewed by resizing  $M_{N3}$  and  $M_{P1}$  to prevent multiple-conduction oscillations. To examine its rectification abilities in low-voltage conditions, the rectifier voltage conversion efficiency (VCE) under open-circuit conditions is simulated in Fig. 4b. The comparison results are also added to highlight the buffer's contribution. The peak VCE is simulated as 99.5%, and the VCE is over 97% when  $V_{PK}$  is larger than 0.4 V. The simulation results meet with the measurement results with errors less than 2%, considering the 10-MΩ probe impedance used in the measurement.

### C. FAC MPPT Detection and Generation

To generate a reference voltage for the fast MPPT, a novel two-step conversion is proposed in this work. As shown in Fig. 5, the differential sine-wave signal  $V_{AC}$  is first converted into a square wave  $V_{trig}$  based on the polarity flip. In the first step, a time-to-voltage converter monitors  $V_{trig}$  and generates an intermediate voltage  $V_{frq}$  which is linearly proportional to  $T_{frq}$ . In the second step, a reciprocal (1/x) converter is activated to generate the final output voltage  $V_{MPPT}$ . The operation principle of the time-to-voltage converter is based on a three-phase (charge-sample-reset) charge-pump introduced in [30]. In the first phase when  $V_{trig}$  is logic low, a 1-nA current source charges up  $C_a$  for the duration of  $T_{frq}$ . In the second phase when  $V_{trig}$  becomes logic high,  $V_c$  is sampled on  $C_{sa}$  via a low leakage switch controlled by  $V_{sha}$ . Finally, in the

third phase with a 400 ns delay after  $V_{sha}$ ,  $C_a$  is reset by  $V_{rst}$  and prepares for the next trigger of  $V_{trig}$ . To accommodate the low-frequency operation down to 10 Hz, a low leakage sample and hold circuit is necessary. An intermediate sample and hold capacitor  $C_{mid}$  is added to alleviate the leakage current from the final output to the ground during the reset phase. By sizing  $C_{mid}$  equal to the sample and hold capacitor  $C_{sa}$  (2 pF), the voltage ripple introduced by the leakage current is less than 15 mV in post-layout simulation. Since  $T_{frq}$  is half of the rotation cycle ( $1/f_{tub}$ ), the DC value of  $V_{frq}$  can be expressed as:

$$V_{frq} = \frac{I_c \times T_{frq}}{C_a} = \frac{I_c}{2 \times f_{tub} \times C_a} \quad (4)$$

Another block is required to generate the MPPT reference by using a reciprocal (1/x) converter. The reciprocal converter is based on capacitor charge conservation principles, and this method requires two reference voltages with two voltage-to-current converters [31], [32]. In this work, only one voltage to current converter is required by replacing the other converter with a ratio current source. In Fig. 5, the multiplied reference current  $I_{ref}$  and the V-I converted current  $I_{in}$  charge the capacitor  $C_1$  and  $C_2$  respectively until the voltage on  $C_1$  reaches the reference voltage  $V_{ref}$ . The voltage on  $C_2$  is then sampled and stored at  $C_{sb}$  (2 pF). In the first step,  $V_{frq}$  is refreshed and hold when  $V_{trig}$  is in low-to-high transition. And in the second step, the  $V_{MPPT}$  is generated and hold from the  $V_{trig}$  when  $V_{trig}$  is logic low. The main signal waveform in simulations is also provided in Fig. 5. All the internal signals are triggered by turbine AC inputs without additional controls. The proposed MPPT method can track the turbine frequency after one cycle in the steady-state.  $V_{MPPT}$  is refreshed by  $V_{trig}$ , and its value is updated from  $V_{frq}$  which was converted in the previous cycle. Meanwhile, the total power consumption for the MPPT reference voltage generation remains as low as 400 nW because of its low frequency and nano-ampere operations. The overall frequency-to-voltage conversion can be derived as:

$$T_{on} = \frac{V_{ref} \times C_1}{G_{V-I} \times V_{in}} \quad (5)$$

$$V_{MPPT} = \frac{M \times I_c \times T_{on}}{C_2} \quad (6)$$

$$\text{Finally, } V_{MPPT} = \frac{2 \times M \times V_{ref} \times C_1 \times C_a}{G_{V-I} \times C_2} \times f_{tub} \quad (7)$$

In (7),  $M$  is the current mirror multiplication ratio.  $V_{\text{ref}}$  is provided from the internal reference voltage.  $G_{V-I}$  is the voltage to current gain in the V-to-I converter which depends on the value of on-chip  $R_{\text{sen}}$ . By sizing  $M$ ,  $G_{V-I}$ ,  $C_a$ ,  $C_1$ , and  $C_2$ , the target linear slope is achieved. In this work,  $M = 10$ ,  $G_{V-I} = 50 \text{ ns}$ ,  $C_a = 40 \text{ pF}$ ,  $C_1 = 150 \text{ pF}$ , and  $C_2 = 34 \text{ pF}$ , which makes target  $\alpha$  numerically equal to  $V_{\text{ref}}$  for design convenience.  $V_{\text{MPPT}}$  is proportional to the ratio of  $C_{a,1,2}$ , and also  $M$ , which provides more immunity to process variations. (7) indicates the simplicity of our proposed method, and this method is also applicable in other frequency-to-voltage conversion applications by selecting the proper parameters. In this work, only  $V_{\text{ref}}$  is reserved to be programmable considering the process variations and adjustments for the different  $\alpha$ .

The proposed FAC MPPT eliminates the drawbacks of the conventional  $V_{\text{OC}}$  detection MPPT in the wind EH applications. To be specific, by measuring  $V_{\text{OC}}$  indirectly, the EH system does not need to be disconnected from the wind turbine, which ensures that energy extraction is uninterrupted and extends the operating range by eliminating high voltage stress under open-circuit conditions. In addition, the loading effect on the WTG induced voltage is decoupled, enabling an accurate and real-time MPPT suitable for wind EH to be achieved while inheriting the low-cost, fast-response merits of the  $V_{\text{OC}}$  detection MPPT.

#### D. Nano-Ampere Peaking Current Source

Although  $I_c$  does not play a role in (7), it is still essential to compromise between the power consumption, capacitor size, and the internal voltage range. Therefore, a constant reference current helps to improve system robustness against PVT variance. A peaking current topology operating in weak inversion regions is employed for its supply independence and capability of operating under low current levels [33]. To achieve a first-order temperature compensation without extra penalty, an N-Well under a diffusion resistor with a positive temperature coefficient (TC) of  $65 \Omega/\text{^{\circ}C}$  and a silicided N+ poly resistor with a negative TC of  $-42 \Omega/\text{^{\circ}C}$  are used to achieve mutual compensation after proper sizing. The designed nominal reference current is  $6 \text{ nA}$  at room temperature. This nano-ampere current reference has a simulated low TC of  $208 \text{ ppm}/\text{^{\circ}C}$  and a small supply sensitivity of  $0.55 \text{ nA/V}$ .

Overall, the static voltage of  $V_{\text{MPPT}}$  is plotted in Fig. 6a. To cover different target  $\alpha$  values, the wide tuning-range is achieved by merely adjusting  $V_{\text{ref}}$ . For example, when  $V_{\text{ref}} = 0.5 \text{ V}$ , the achieved  $\alpha$  ranges from  $0.45$  to  $0.47$  with an average error of  $7.6\%$ . The maximum  $V_{\text{MPPT}}$  deviation is  $10\%$ , and the overall efficiency difference is less than  $3\%$ . When necessary, the deviation can be further minimized by fine-tuning  $V_{\text{ref}}$ . Fig. 6b shows the Monte-Carlo simulation results with an intermediate  $f_{\text{tub}} = 20 \text{ Hz}$ . It is noted that the current and voltage reference, LDO, and the entire FAC MPPT circuits are included in the simulation. The target  $V_{\text{MPPT}}$  is  $0.7 \text{ V}$ , and the generated mean value is  $715 \text{ mV}$  with a standard deviation of  $47 \text{ mV}$ . By replacing the other V-to-I converter in the reciprocal block with the multiplied ratio current branch ( $I_{\text{ref}} = M \times I_c$ ), the deviation in  $V_{\text{MPPT}}$  is reduced by  $30\%$ , and the silicon area is compressed by  $20\%$ .

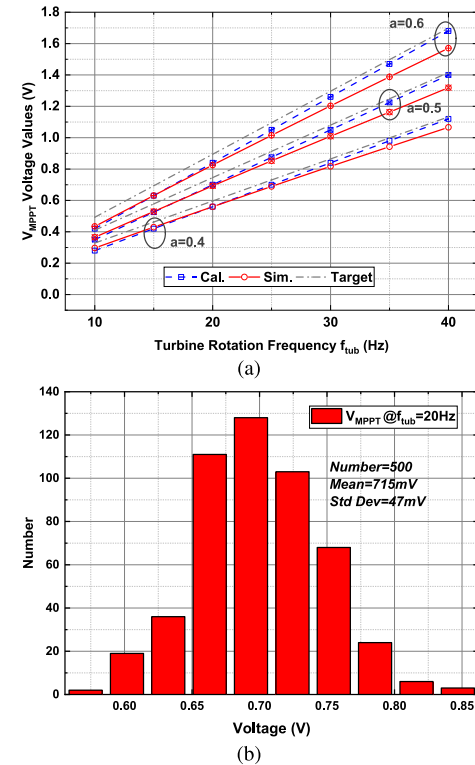


Fig. 6. Static  $V_{\text{MPPT}}$  in simulations (a)  $V_{\text{ref}} = 0.4, 0.5$ , and  $0.6 \text{ V}$  respectively, (b) Monte-Carlo simulation results when  $f_{\text{tub}} = 20 \text{ Hz}$ . ( $\alpha = 0.5$ ).

#### E. Boost Converter for MPPT Power Extraction

Fig. 7 shows the boost converter architecture with the supportive unit blocks. The boost converter ensures that the loading voltage of the rectifier is near its optimal value for maximum power extractions and boosts up the final output voltage. An MPPT comparator triggers the boost converter with hysteresis-control. The whole system operates asynchronously without any additional clocking or control elements. The quiescent current of the boost converter is measured as  $20 \text{ nA}$  in the idle state when the input is zero (the MPPT comparator is disabled when  $V_{\text{PG}} = 0$ ), and the operation power consumption is from  $10$  to  $30 \mu\text{W}$ , which is adaptive to the input power levels. In this work, the boost converter is used for MPPT energy extraction. Although the loading is not regulated, the FAC MPPT algorithm is immune to different loading conditions by monitoring the real-time turbine frequency as analyzed in Section II. For output loading regulation, many recent works in EH-PMU have proposed advanced techniques [34]–[36].

To regulate the rectifier's output voltage around the desired maximum power point, a hysteresis control is implemented for its simplicity and inherent stability by a nA-biased comparator. The hysteresis window is around  $2 \mu\text{s}$  with a switching frequency around  $50 \text{ KHz}$  according to the simulation. The control signal  $V_{\text{LS}}$  of the low-side (LS) NMOS switch also serves as the trigger signal for the following zero-current-switching (ZCS) operations. Therefore, the boost converter operates under asynchronous control, requiring no additional clocking circuit, which simplifies the design and minimizes the consumed power in the idle phase.

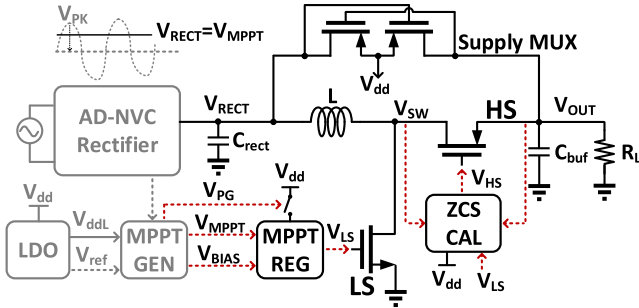


Fig. 7. Boost Converter for power conversion and MPPT.

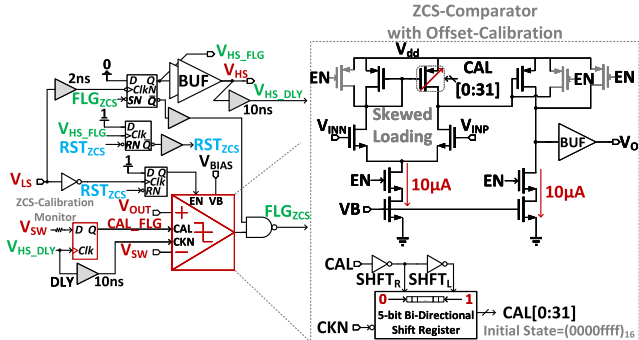


Fig. 8. ZCS controller with comparator offset automatic self-calibration.

To deliver all the available charge stored in the inductor, the high-side (HS) switch is controlled by the ZCS technique [37]. The conventional ZCS uses a high-speed comparator operating only in the HS phase to alleviate the power-speed trade-off. A predefined offset in this comparator is also required to compensate for the path delay. However, the offset is also sensitive to PVT variations. Therefore, the ZCS controller with calibration is employed to achieve high efficiency [38]–[40]. To address this issue, an asynchronous digital calibration technique is implemented by additional arbitration after the ZCS cycle is finished. The complete ZCS controller is shown in Fig. 8. The ZCS comparator is enabled by  $V_{LS}$  with a delay of 2 ns. The ZCS comparator detects the voltage difference between  $V_{SW}$  and  $V_{OUT}$  and turns off the HS switch when  $V_{SW}$  reaches  $V_{OUT}$ , which means the charge transfer is finished. Then the ZCS comparator itself is deactivated to save power until the next trigger signal.

To ensure optimal ZCS, the offset of the ZCS comparator needs to be controlled to provide a timely response. A digital flip-flop (DFF) serves as the arbiter circuit to automatically detect the voltage level of  $V_{SW}$  after ZCS with a predefined delay signal  $V_{HS\_DLY}$ . If the HS switch is turned off too early when the charging current is still positive,  $V_{SW}$  will be charged up higher than  $V_{OUT}$  after ZCS. And if the HS switch is turned off too late when the charging current is already negative, then  $V_{SW}$  will be discharged lower than GND [38]. Therefore, a simple DFF is sufficient to arbitrate the performance of ZCS with an ESD-protection resistor. A 5-bit offset automatic self-calibration is employed in the ZCS comparator to provide a unified offset tuning by controlling the active loading devices [41]. The tuning-range is from  $-40$  to  $68$  mV with an average step resolution of  $3.5$  mV.

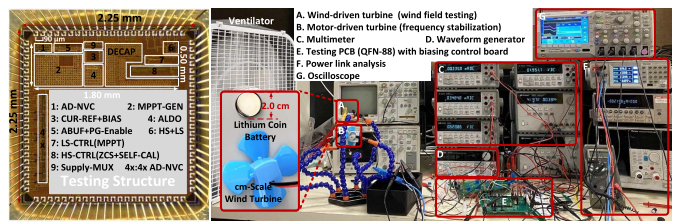


Fig. 9. (a) Chip micro-photograph with test-bench and (b) testing schematic.

The offset in the central state (Digital Code 15) is skewed to compensate for the path delay.

In addition to the circuits for energy delivery, an external capacitorless LDO provides a 1.5 V voltage supply and a programmable reference voltage from 0.2 to 0.6 V by the resistor dividers. The quiescent current of LDO is 40 nA. A maximum supply voltage selector assists in the system start-up. Two cross-coupled PMOS transistors feed the  $V_{dd}$  with the maximum voltage between  $V_{RECT}$  and  $V_{OUT}$  automatically. The supply multiplexer automatically charges up the internal  $V_{dd}$  through the rectifier output voltage until the normal operation mode is activated. Furthermore, before the  $V_{dd}$  is fully charged up, the boost converter is disabled until the power-good signal  $V_{PG}$  is generated. The  $V_{PG}$  generation circuit is based on digital flip-flops comparator [42], where  $V_{trig}$  serves as the clock.

### III. MEASUREMENT RESULTS

The EH system is fabricated in CMOS 180-nm technology. The active area is  $0.9\text{ mm}^2$ , and a  $4\times$ -area AD-NVC rectifier is also fabricated as a counterpart for performance comparisons. The off-the-shelf components include  $\mu\text{F}$ -level loading capacitors and a  $47\text{-}\mu\text{H}$  inductor. The chip micro-photograph is shown in Fig. 9, together with the testing setup details. A PA1000 AC power analyzer and 34401A multimeters monitor the critical voltage and current information in the power delivery path. A 6487 picoammeter records the system consumed current. A 33120A waveform generator injects the well-defined AC input signal to test the MPPT response. And an MSO2024B multi-channel oscilloscope captures the signal waveform for MPPT demonstrations. The volume of the turbine is  $8\text{ cm}^3$  with a 2.5-cm radius wind blade. A ventilator with a handheld wind-speed measurement instrument is used to characterize the EH system performance in wind field-testing. Meanwhile, a DC-motor directly drives the turbine for testing under stabilized rotation frequencies, thereby providing the driving power needed to overcome the demanding torque under different loading conditions.

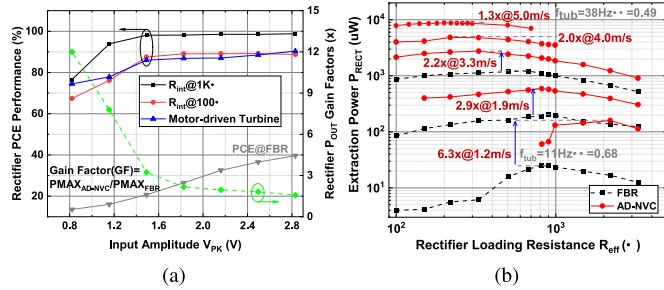


Fig. 10. Rectifier (a) PCE tested in motor-driven testing, (b) harvested output power in wind-field testing.

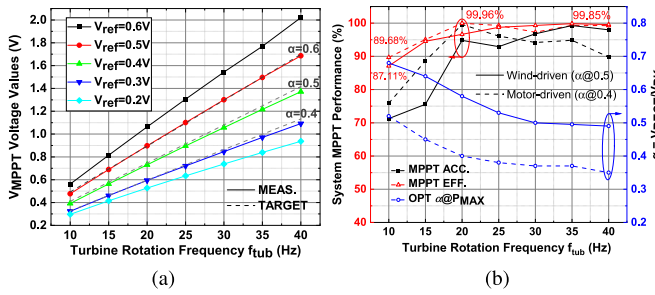


Fig. 11. (a)  $V_{MPPT}$  static output voltage, (b) MPPT performance.

Before quantifying the overall performance, the individual performance of each block is first examined. The power conversion efficiency (PCE) of the AD-NVC rectifier is plotted in Fig. 10a. When  $R_{int} = 1\text{ K}\Omega$ , the power conversion efficiency (PCE) of the AD-NVC is above 94% when  $V_{PK}$  is larger than 1.2 V, indicating its high efficiency for low-voltage and  $\mu\text{Watt}$ -level EM applications. The PCE performance drops to 89% when  $R_{int} = 100\text{ }\Omega$  because of the larger conduction loss. To quantify the power extraction abilities, the achievable energy extraction gain compared to a conventional Schottky-diode-based (RB520S,  $V_F = 280\text{ mV}$  at 1 mA) full-bridge rectifier (FBR) is also shown in Fig. 10a. The PCE of FBR is relatively low ( $< 40\%$ ) for the whole range because the  $V_F$  is comparable with the target rectifier output voltage (0.4 – 1.4 V) at the MPP. Under the same  $V_{PK}$ , the output power of the AD-NVC rectifier is 12× compared to the FBR in the low-frequency range, indicating its outstanding performance, especially in low-voltage domains. In Fig. 10b, the performance comparison is also conducted with similar wind speed conditions. To overcome the undesired wind speed fluctuation, the turbine rotation frequency is monitored to ensure a fair comparison. The AD-NVC achieves a 6.3× extracted output power gain in low-wind conditions at 1.2 m/s, while still maintaining at 2.0× in 4.0 m/s. Notably, the optimal loading  $R_{eff}$  is larger in the wind-field testing compared to the motor-driven testing, which is due to the loading effect on WTG discussed in Section II.

The  $V_{MPPT}$  under  $V_{ref}$  from 0.2 V to 0.6 V is plotted in Fig. 11a. The results show a wide tuning ability and a feasible tuning solution in the proposed FAC MPPT, which makes the  $V_{MPPT}$  applicable for other frequency-to-voltage conversion applications, such as low-cost wind-speed detection. With the  $V_{ref}$  value trimmed down by 100 mV, an accuracy above 95% is achieved compared to target  $\alpha$ . Therefore, as characterized in Fig. 11b, an  $\alpha$  of 0.4 ensures the optimal

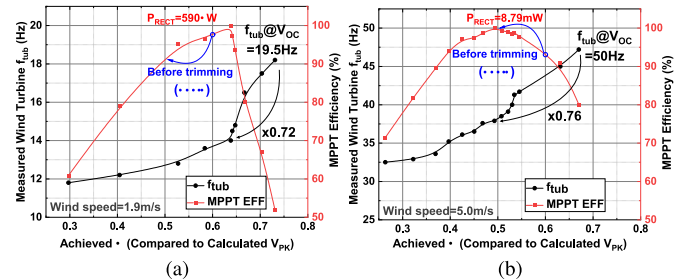


Fig. 12.  $P_{RECT}$  with different  $\alpha$  under (a) a low wind-speed condition (1.9 m/s) (b) a high wind-speed condition (5.0 m/s).

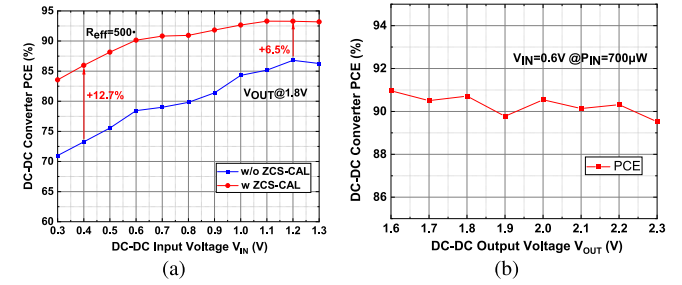


Fig. 13. DC-DC converter PCE versus (a) input voltage, (b) output voltage.

MPPT performance in the motor-driven testing. Meanwhile, an  $\alpha$  of 0.5 maximizes the MPPT performance in the wind-driven testing, which achieves a peak MPPT efficiency (ratio to the maximum output power) of 99.85% with an MPPT accuracy (ratio to the optimal MPPT voltage) of 99.27%. Although the FAC MPPT circuit parameters are designed and optimized for the target wind turbine, the MPPT algorithm is applicable for any other rotary EM turbines with proper calibrations or parameter adjustments. The variance of an optimal  $\alpha$  also depicts the necessity of tuning  $\alpha$  values for different EH scenarios. The optimal  $\alpha$  is close to 0.4 in the motor-driven testing because the turbine is represented as an ideal voltage source without any loading effects. However, in wind-driven testing, the torque equilibrium acts as an additional loss and leads to a higher optimal  $\alpha$ . Notably, the motor-driven conditions can represent EH applications for ocean waves or marine current where the EH driven-torque is dominant [43].

In Fig. 12a and 12b, the normalized AD-NVC output power under different wind-field testing are plotted with different achieved  $\alpha$ . In general, an  $\alpha$  from 0.5 to 0.6 can achieve an overall MPPT efficiency larger than 90%. Before trimming  $V_{ref}$ , the achieved  $\alpha$  is close to 0.6, which is preferred in low wind speed (1 – 2 m/s) conditions. Overall, the corresponding MPPT efficiency before trimming is ranged from 88% to 97%. The changes in  $f_{tub}$  are also plotted with different loading conditions ( $\alpha$ ). The decrease of rotation frequency justifies the previous analysis in Section II.

The PCE of the DC-DC converter is shown in Fig. 13. A 200-mΩ low-DCR 47-μH shielded inductor is selected for low cost and high efficiency. Thanks to the contribution of the self-calibration technique in the ZCS, the PCE of the boost converter is maintained above 90% for a wide input voltage ranging from 0.6 V, and the output voltage covers from 1.6 V to 2.2 V, which achieves a 12.7% peak performance improvement compared to the performance when self-calibration

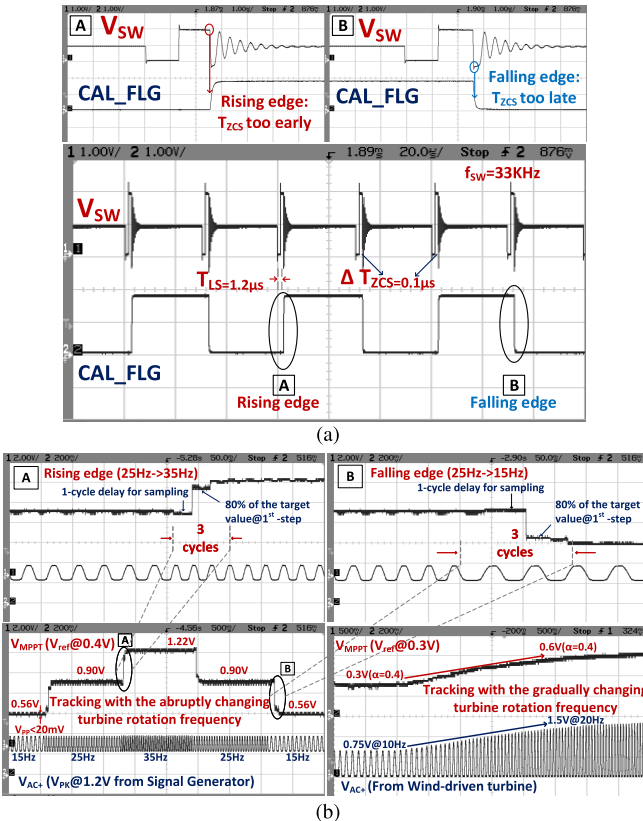


Fig. 14. The transient waveform of (a) ZCS self-calibration, (b) MPPT response.

is disabled. The transient steady state of the ZCS self-calibration is plotted in Fig. 14a. The optimal ZCS point is locked by two back-and-forth digital states, with a  $0.1 \mu\text{s}$  resolution in the adjacent state. Although the ringing appears after ZCS, the HS reverse recovery time is larger than 200 ns after the self-calibration, so it does not affect the system operations. This ringing is common in boost converter in the discontinuous conduction mode (DCM) since the  $V_{\text{sw}}$  is floating when LS and HS switches are both disabled. In this work, the ringing is minimized by reducing the parasitic capacitance of  $V_{\text{sw}}$  to make its amplitude smaller than the rated voltage level.

Fig. 14b demonstrates the  $V_{\text{MPPT}}$  response with different types of frequency changes. First, the MPPT response under abrupt frequency changes is tested. The input sinusoidal signal is generated from a signal generator with a step frequency of 10 Hz. The zoom-in plot shows that the proposed MPPT method can track the abrupt frequency change within three turbine cycles, with an 80% accuracy in the first turbine cycle. When tested with the gradually changing wind-driven turbine, the cycle-to-cycle amplitude  $V_{\text{PK}}$  difference is less than 2%; meanwhile, the  $V_{\text{MPPT}}$  can still track this small change smoothly. The high-resolution capability is maintained while the fast response is also achieved by the variable and adaptive step response. The  $V_{\text{MPPT}}$  is triggered by the turbine operation itself. Therefore, no additional clocking element or control circuits are required. The whole interface IC, including the AD-NVC rectifier, the MPPT functions, and the DC-DC converter, operates autonomously in favor of modular designs.

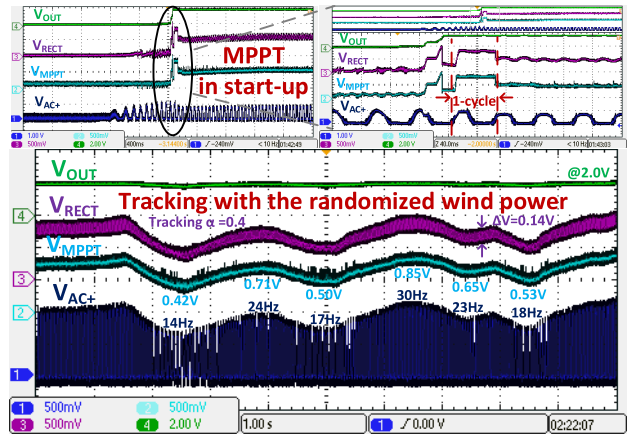


Fig. 15. The system with MPPT in a wind field-testing demonstration.

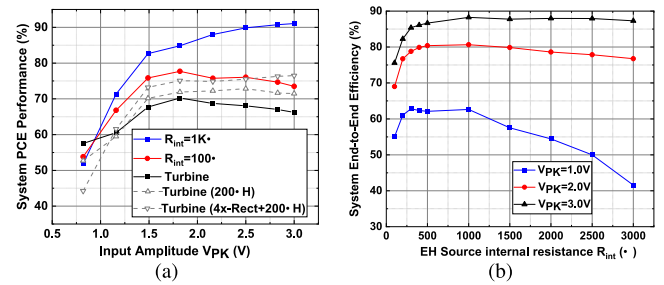


Fig. 16. System performance of (a) PCE with motor-driven testing ( $f_{\text{tub}}$  changes with  $V_{\text{PK}}$ , w/ FAC-MPPT), (b) End-to-end EFF with well-defined AC source (Fixed frequency = 40 Hz,  $\alpha = 0.4$  w/o FAC-MPPT).

The system tested in an actual wind field is shown in Fig. 15. The loading is a  $10-\mu\text{F}$  capacitor with a  $5-\text{K}\Omega$  resistance. After the system is stabilized at 2.0 V from start-up, the correct  $V_{\text{MPPT}}$  is generated after one turbine cycle, demonstrating the ability of the MPPT to operate in shock or burst modes. For fast varying wind power,  $V_{\text{MPPT}}$ ,  $V_{\text{RECT}}$ , and  $V_{\text{AC}+}$  are tracking the turbine frequency from cycle to cycle. As previously mentioned, different loading conditions affect the operations of the EM turbine and introduce errors in conventional open-circuit detection methods. However, the proposed FAC MPPT monitors the turbine frequency  $f_{\text{tub}}$  in real-time. The envelope depicts the dynamic and accurate response of the proposed MPPT operations in different wind EH scenarios, such as the continuous and shock excitation. The adaptive FAC MPPT monitors the turbine rotation frequency without interrupting the energy transfer, which means all the available energy is extracted and delivered to the loading under dynamically changing wind conditions.

In Fig. 16a, the overall system PCE is measured in motor-driven testing, which is defined by the percentage of the output power compared to the average AC input power. The AC input power is measured by an AC/DC power analyzer. With a well-defined  $R_{\text{int}}$  source, the peak PCE is 91% when  $R_{\text{int}} = 1 \text{ K}\Omega$ , while the peak PCE is 77.7% with a smaller  $R_{\text{int}} = 100 \Omega$ . The PCE is dropped down mainly because of the conduction loss with the increasing conduction current reaching up to 10 mA. When tested with the turbine, the peak PCE is 70% when  $V_{\text{PK}} = 1.8 \text{ V}$ , which is also degraded compared to the well-defined  $R_{\text{int}}$  source. However, in wind field-testing, the PCE performance in the practical

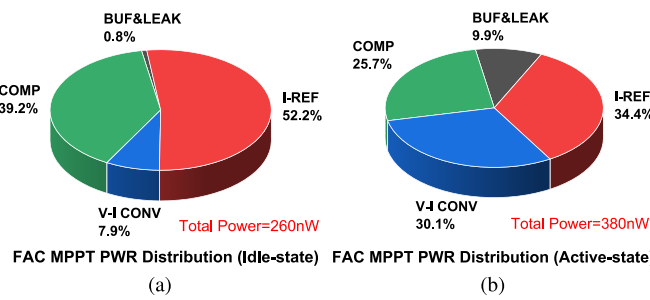


Fig. 17. FAC MPPT consumed power distributions in (a) Idle state with zero input, (b) Activated state. total power is based on measurement, power distribution is based on simulation.

implementation is between  $R_{int} = 1000 \Omega$  and  $R_{int} = 100 \Omega$  in two cases. An alternative rectifier with a quadruple area coverage can improve the overall system performance by 5% if PCE improvement is demanded. Meanwhile, a larger inductor of  $200-\mu\text{H}$  can also help in the large  $V_{PK}$  conditions by reducing the peak inductor current. The peak PCE is improved by 10% with a performance degradation of 13.3% in low power domains, showing the design trade-off for the low cost (area and form factors) and optimal PCE for different operation ranges. In Fig. 16b, the end-to-end efficiency (EFF) is characterized by changing  $R_{int}$  [19]. The end-to-end EFF is determined by the PCE performance and the power extraction ability (MPPT efficiency). However, for measurement convenience, the input AC frequency is fixed at 40 Hz with an external  $V_{MPPT}$  voltage to ensure  $\alpha = 0.4$  since the MPPT efficiency has been examined in Fig. 11 with accurate  $\alpha$ -tracking abilities. A peak end-to-end EFF is measured as 88.2% when  $V_{PK} = 3.0 \text{ V}$ , and it is kept as 62.8% with low  $V_{PK} = 1.0 \text{ V}$ , indicating the high efficiency is still reserved in low-voltage and  $\mu\text{W}$  EH applications. The EFF is dropped down at low input power domains mainly because the minimum DC-DC converter operation power is  $8 \mu\text{W}$ . Wind-driven testing cannot provide stable wind power for the end-to-end system performance evaluations (PCE and end-to-end EFF). In future works, more accurate results can be achieved with a wind tunnel test. Nevertheless, the high end-to-end EFF with different  $R_{int}$  implies the system's potentials with different micro wind turbines.

In Fig. 17, the power distribution of FAC MPPT is extracted and plotted. In the idle mode, since the DC-DC converter is disabled, the entire system power consumption is dominated by the FAC MPPT circuit. The power consumption of current and voltage reference occupies over 50% in this state. In the activated state, the power consumption of the FAC MPPT circuit remains at low power as 380 nW because of low-speed operations. However, in this state, the entire system power is dominated by the boost converter operations. The typical DC-DC converter power consumption in the activated state is  $10 \mu\text{W}$ : 20% by the MPPT controller, 38% by the ZCS controller, and 42% by the buffers and leakages.

Table I draws a comparison with other EM or AC-type EH systems with comparable output power or input voltage. The presented system achieves fast and wide range MPPT for cycle-to-cycle tracking with an ultra-low-power consumption of 380 nW, and an MPPT processing efficiency larger than 99.6%. A  $20\times$  smaller inductor ( $47-\mu\text{H}$ ) is selected for

TABLE I  
SYSTEM PERFORMANCE COMPARED TO STATE-OF-ARTS

References	[18]	[19]	[20]	[4]	[3]	This work
Process	350nm BCD	350nm	350nm	Discrete	Discrete	180nm
Active Area	$4.7\text{mm}^2$	$1.3\text{mm}^2$	$1.3\text{mm}^2$	NA	NA	$0.9\text{mm}^2$
E-H Type	EM/PEH	EM	EM	EM turbine	EM turbine	EM turbine
$E-H F_{SR}$	100-400 Hz	64, 109 Hz	70 Hz	NA	10-100 Hz	<b>10-40 Hz</b>
Architecture	Act. Rect. +Buck-Boost	NVC+AD +Boost	Doubler +Boost	Act. Rect. +Buck-Boost	Act. Rect. +Boost	AD-NVC +Boost
Inductor	10 mH	1 mH	3.3 mH	NA	10 mH	$47\text{-}\mu\text{H}$
Out. Power	0.03-10 mW	0.004-1 mW	40-200 $\mu\text{W}$	2.30 mW	1-70 mW	<b>0.1-8 mW</b>
Out. Voltage	1-8 V	4.2 V	3.3 V	5.0 V	3.0 V	<b>1.6-2.0 V</b>
MPPT Method	$V_{OC}$ Detect.	Conduction Angle	Auxiliary EM source	Varied $F_{sw}$ $V_{OC}$ Detect.	$R_{LOAD}$ Emulation	<b>Freq-to-V<sub>PK</sub> Conversion</b>
MPPT-GEN PWR (EFF*)	$10 \mu\text{W}$ (66.7%)	$40 \text{nW}$ (99.0%)	NA. (50%)	NA. (with MCU)	$267 \mu\text{W}$ (73.3%)	<b>380 nW (99.6%)</b>
MPPT-Cycle Worst Case	Infinity (Fixed $F_{sw}$ )	$\Delta V/0.05$ ( $20\text{mV}/\Delta V=1\text{V}$ )	=1 (Always-on)	Infinity	=1 (Always-on)	<3 (>80%@1 <sup>st</sup> step)
Cycle-to-cycle MPPT	NO	NO	YES	NO	NO	<b>YES</b>
Voltage Stress	High@ $V_{OC}$	LOW	High	NA.	NA.	<b>LOW</b>
MPPT EFF.	$\eta_p=99.0\%$	$\eta_p=90\%$	$\eta_p=93\%$	NA.	NA.	$\eta_p=99.85\%$
Peak EFF (End-to-End)	80% (only buck-boost)	95%@ $V_{PK}=3.6\text{V}$	72%@ $V_{PK}=1.7\text{V}$ (w/o Aux. EM)	82%@ $V_{PK}=10.0\text{V}$	60%@ $V_{PK}=10.0\text{V}$	<b>88.2%@ <math>V_{PK}=3.0\text{V}</math></b>
EFF @ $V_{PK}=1.0\text{V}$	NA.	50%	69% (w/o Aux. EM)	<30%	NA.	<b>62.8%</b>
Rectification FoM* (Periodic)	NA.	NA.	NA.	<1.3x	$1.2x$ @ $8.5\text{m/s}$ $V_{PK}=8.5\text{V}$ $3.0x$ @ $2.3\text{m/s}$ $V_{PK}=1.5\text{V}$	<b>1.3x @<math>5.0\text{m/s}</math> <math>V_{PK}=2.7\text{V}</math> <math>6.3x</math> @<math>1.2\text{m/s}</math> <math>V_{PK}=0.9\text{V}</math></b>

\*MPP-GEN EFF=(1-MPPT-GEN/P<sub>OUT(MIN)</sub>) \*100%, the MPP information processing efficiency

\*\*FoM=P<sub>OUT(MAX)</sub>/AD-NVC/P<sub>OUT(MAX)</sub>/FBR, the energy extraction gain

reduced form factor and low-cost design. The whole system including the rectifier design is optimized for autonomous and sub-1V operations, achieving a 630% energy extraction gain at low wind-speed conditions of 1.2 m/s ( $V_{PK} = 0.9 \text{ V}$ ). Compared to [19], the proposed system achieves a comparable peak end-to-end EFF with less active silicon area and a smaller inductor, while an 8 $\times$  power delivery ability is achieved. Moreover, the proposed FAC MPPT achieved cycle-to-cycle MPPT with a fast and adaptive response, while maintaining the least power overhead compared to the harvested power [3], [18]. The work in [20] achieves better EFF performance in low voltage domains because of the voltage boost gain in AC-DC doubler circuits. However, its MPPT algorithm relies on an auxiliary EM source, which increases the system form factor and degrades the overall effective end-to-end EFF by half if the available energy in this auxiliary EM source is considered. In this work, the highest MPPT efficiency was also achieved with wide-tuning abilities for the wide-range operations from 10 to 40 Hz (4 $\times$ ). Moreover, the cycle-to-cycle MPPT ability locates the optimal MPP with only one operation cycle to accommodate the unpredictable wind speed conditions, which advances most of the existing low-cost wind MPPT solutions with ultra-low-power consumption. The harvested wind speed is covered from 1.0 to 5.0 m/s. The minimum MPPT operation range is extended by 2.3 $\times$  compared to [3], which is limited by the minimum cut-in wind speed of the wind turbine itself. To provide output loading regulation, an additional LDO can be added. However, it will reduce the end-to-end efficiency. An additional switching converter [3], [4] could also be implemented, with extra components and cost. Depending on system requirements, multiple-path topologies [37]–[40] can also be incorporated into the design. Optimization of an EH system for simultaneous MPPT energy extraction and voltage regulation is still a challenging topic deserving further research.

## IV. CONCLUSION

This work presented a power-efficient system for the EM wind turbine EH. The system is optimized for a wide input power range with self-start-up and autonomous operations. Furthermore, the proposed FAC MPPT maximizes the power extraction ability under different wind conditions from 1.0 to 5.0 m/s. The fast cycle-to-cycle MPPT transient response and short settling time (one cycle) can ensure that the EH system is suitable for continuous energy extraction, as well as the shock or burst excitation. The total quiescent current of the EH system is 230 nA when the wind power is absent. To the best of the authors' knowledge, this is the first IC prototype for a cm-scale wind turbine EH which achieves a real-time MPPT with the highest reported MPPT efficiency. The proposed FAC MPPT design is low cost with wide-tuning abilities, suitable for other linear frequency-to-voltage conversion applications, such as low-cost wind speed detection.

## REFERENCES

- [1] M. Habibzadeh, M. Hassanaliagh, A. Ishikawa, T. Soyata, and G. Sharma, "Hybrid solar-wind energy harvesting for embedded applications: Supercapacitor-based system architectures and design tradeoffs," *IEEE Circuits Syst. Mag.*, vol. 17, no. 4, pp. 29–63, Nov. 2017.
- [2] Y. K. Tan and S. K. Panda, "Self-autonomous wireless sensor nodes with wind energy harvesting for remote sensing of wind-driven wildfire spread," *IEEE Trans. Instrum. Meas.*, vol. 60, no. 4, pp. 1367–1377, Apr. 2011.
- [3] Y. K. Tan and S. K. Panda, "Optimized wind energy harvesting system using resistance emulator and active rectifier for wireless sensor nodes," *IEEE Trans. Power Electron.*, vol. 26, no. 1, pp. 38–50, Jan. 2011.
- [4] D. Porcarelli, D. Spenza, D. Brunelli, A. Cammarano, C. Petrioli, and L. Benini, "Adaptive rectifier driven by power intake predictors for wind energy harvesting sensor networks," *IEEE J. Emerg. Sel. Topics Power Electron.*, vol. 3, no. 2, pp. 471–482, Jun. 2015.
- [5] E. Sardini and M. Serpelloni, "Self-powered wireless sensor for air temperature and velocity measurements with energy harvesting capability," *IEEE Trans. Instrum. Meas.*, vol. 60, no. 5, pp. 1838–1844, May 2011.
- [6] P. D. Mitcheson, E. M. Yeatman, G. K. Rao, A. S. Holmes, and T. C. Green, "Energy harvesting from human and machine motion for wireless electronic devices," *Proc. IEEE*, vol. 96, no. 9, pp. 1457–1486, Sep. 2008.
- [7] S. Nabavi and L. Zhang, "Portable wind energy harvesters for low-power applications: A survey," *Sensors*, vol. 16, no. 7, p. 1101, Jul. 2016.
- [8] L. Zhao and Y. Yang, "Toward small-scale wind energy harvesting: Design, enhancement, performance comparison, and applicability," *Shock Vibrat.*, vol. 2017, pp. 1–31, Jan. 2017.
- [9] M. M. Ababneh, S. Perez, and S. Thomas, "Optimized mini notched turbine energy harvesting using resistor emulation approach and particle swarm optimization," in *Proc. SoutheastCon*, Mar. 2017, pp. 1–6.
- [10] N. Rezaei-Hosseiniabadi, A. Tabesh, and R. Dehghani, "A topology and design optimization method for wideband piezoelectric wind energy harvesters," *IEEE Trans. Ind. Electron.*, vol. 63, no. 4, pp. 2165–2173, Apr. 2016.
- [11] J. E. D. P. Braquehais and A. A. L. de Souza, "Energy-autonomous wind speed smart sensor," in *Proc. IEEE Int. Instrum. Meas. Technol. Conf. (I2MTC)*, May 2014, pp. 931–935.
- [12] D. Brunelli, "A high-efficiency wind energy harvester for autonomous embedded systems," *Sensors*, vol. 16, no. 3, p. 327, Mar. 2016.
- [13] F. Deng, X. Yue, X. Fan, S. Guan, Y. Xu, and J. Chen, "Multisource energy harvesting system for a wireless sensor network node in the field environment," *IEEE Internet Things J.*, vol. 6, no. 1, pp. 918–927, Feb. 2019.
- [14] B. Pozo, J. Á. Araujo, H. Zessin, L. Mateu, J. I. Garate, and P. Spies, "Mini wind harvester and a low power three-phase AC/DC converter to power IoT devices: Analysis, simulation, test and design," *Appl. Sci.*, vol. 10, no. 18, p. 6347, Sep. 2020.
- [15] Z. M. Dalala, Z. U. Zahid, W. Yu, Y. Cho, and J.-S. Lai, "Design and analysis of an MPPT technique for small-scale wind energy conversion systems," *IEEE Trans. Energy Convers.*, vol. 28, no. 3, pp. 756–767, Sep. 2013.
- [16] P.-C. Huang, Y.-C. Kuo, Y.-C. Liu, and T.-H. Kuo, "An analog optimum torque control IC for a 200-W wind energy harvesting system," *IEEE Trans. Circuits Syst. II, Exp. Briefs*, vol. 66, no. 11, pp. 1790–1794, Nov. 2019.
- [17] G. Revel, A. E. Leon, D. M. Alonso, and J. L. Moiola, "Dynamics and stability analysis of a power system with a PMSG-based wind farm performing ancillary services," *IEEE Trans. Circuits Syst. I, Reg. Papers*, vol. 61, no. 7, pp. 2182–2193, Jul. 2014.
- [18] M. Shim, J. Kim, J. Jeong, S. Park, and C. Kim, "Self-powered 30  $\mu$ W to 10 mW piezoelectric energy harvesting system with 9.09 ms/V maximum power point tracking time," *IEEE J. Solid-State Circuits*, vol. 50, no. 10, pp. 2367–2379, Oct. 2015.
- [19] J. Leicht and Y. Manoli, "A 2.6  $\mu$ W-1.2 mW autonomous electromagnetic vibration energy harvester interface IC with conduction-angle-controlled MPPT and up to 95% efficiency," *IEEE J. Solid-State Circuits*, vol. 52, no. 9, pp. 2448–2462, Feb. 2017.
- [20] J. Leicht, D. Maurath, and Y. Manoli, "Autonomous and self-starting efficient micro energy harvesting interface with adaptive MPPT, buffer monitoring, and voltage stabilization," in *Proc. ESSCIRC (ESSCIRC)*, Sep. 2012, pp. 101–104.
- [21] J.-C. Hsieh and T.-H. Tsai, "An AC-DC wind energy harvesting circuit with extended input-voltage range and 95% tracking efficiency," in *Proc. IEEE Int. Symp. Circuits Syst. (ISCAS)*, May 2018, pp. 1–4.
- [22] A. Quelen, G. Pillonnet, P. Gasnier, F. Rummens, and S. Boisseau, "32.3 electromagnetic mechanical energy-harvester IC with no off-chip component and one switching period MPPT achieving up to 95.9% end-to-end efficiency and 460% energy-extraction gain," in *IEEE Int. Solid-State Circuits Conf. (ISSCC) Dig. Tech. Papers*, Feb. 2020, pp. 490–492.
- [23] Y.-J. Hu, I.-C. Chen, and T.-H. Tsai, "A piezoelectric vibration energy harvesting system with improved power extraction capability," in *Proc. IEEE Asian Solid-State Circuits Conf. (A-SSCC)*, Nov. 2016, pp. 305–308.
- [24] Y. Rao and D. P. Arnold, "An input-powered vibrational energy harvesting interface circuit with zero standby power," *IEEE Trans. Power Electron.*, vol. 26, no. 12, pp. 3524–3533, Dec. 2011.
- [25] C. Peters, J. Handwerker, D. Maurath, and Y. Manoli, "A sub-500 mV highly efficient active rectifier for energy harvesting applications," *IEEE Trans. Circuits Syst. I, Reg. Papers*, vol. 58, no. 7, pp. 1542–1550, Jul. 2011.
- [26] Y.-H. Lam, W.-H. Ki, and C.-Y. Tsui, "Integrated low-loss CMOS active rectifier for wirelessly powered devices," *IEEE Trans. Circuits Syst. II, Exp. Briefs*, vol. 53, no. 12, pp. 1378–1382, Dec. 2006.
- [27] C. Lu, C.-Y. Tsui, and W.-H. Ki, "Vibration energy scavenging system with maximum power tracking for micropower applications," *IEEE Trans. Very Large Scale Integr. (VLSI) Syst.*, vol. 19, no. 11, pp. 2109–2119, Nov. 2011.
- [28] C. van Liempd, S. Stanzione, Y. Allassameh, and C. van Hoof, "A 1  $\mu$ W-to-1 mW energy-aware interface IC for piezoelectric harvesting with 40nA quiescent current and zero-bias active rectifiers," in *IEEE Int. Solid-State Circuits Conf. (ISSCC) Dig. Tech. Papers*, Feb. 2013, pp. 76–77.
- [29] A. Costilla Reyes, A. Abuellil, J. J. Estrada-Lopez, S. Carreon-Bautista, and E. Sanchez-Sinencio, "Reconfigurable system for electromagnetic energy harvesting with inherent activity sensing capabilities for wearable technology," *IEEE Trans. Circuits Syst. II, Exp. Briefs*, vol. 66, no. 8, pp. 1302–1306, Aug. 2019.
- [30] A. Djemouai, M. A. Sawan, and M. Slamani, "New frequency-locked loop based on CMOS frequency-to-voltage converter: Design and implementation," *IEEE Trans. Circuits Syst. II, Analog Digit. Signal Process.*, vol. 48, no. 5, pp. 441–449, May 2001.
- [31] B.-D. Yang and S. W. Heo, "Accurate tunable-gain 1/x circuit using capacitor charging scheme," *ETRI J.*, vol. 37, no. 5, pp. 972–978, 2015.
- [32] Y. Gao, L. Li, and P. K. T. Mok, "An AC input inductor-less LED driver for efficient lighting and visible light communication," *IEEE J. Solid-State Circuits*, vol. 53, no. 8, pp. 2343–2355, Aug. 2018.
- [33] M. H. Cheng and Z. W. Wu, "Low-power low-voltage reference using peaking current mirror circuit," *Electron. Lett.*, vol. 41, no. 10, pp. 572–573, May 2005.
- [34] K. Rawy, T. Yoo, and T. T. Kim, "An 88% efficiency 0.1-300- $\mu$ W energy harvesting system with 3-D MPPT using switch width modulation for IOT smart nodes," *IEEE J. Solid-State Circuits*, vol. 53, no. 10, pp. 2751–2762, 2018.
- [35] J. Jeong, M. Shim, J. Maeng, I. Park, and C. Kim, "A high-efficiency charger with adaptive input ripple MPPT for low-power thermoelectric energy harvesting achieving 21% efficiency improvement," *IEEE Trans. Power Electron.*, vol. 35, no. 1, pp. 347–358, Jan. 2020.

- [36] X. Liu, K. Ravichandran, and E. Sanchez-Sinencio, "A switched capacitor energy harvester based on a single-cycle criterion for MPPT to eliminate storage capacitor," *IEEE Trans. Circuits Syst. I, Reg. Papers*, vol. 65, no. 2, pp. 793–803, Feb. 2018.
- [37] A. Shrivastava, Y. K. Ramadas, S. Khanna, S. Bartling, and B. H. Calhoun, "A  $1.2\mu\text{W}$  SIMO energy harvesting and power management unit with constant peak inductor current control achieving 83–92% efficiency across wide input and output voltages," in *Proc. Symp. VLSI Circuits Dig. Tech. Papers*, Jun. 2014, pp. 1–2.
- [38] S. Carreon-Bautista, A. Eladawy, A. N. Mohieldin, and E. Sanchez-Sinencio, "Boost converter with dynamic input impedance matching for energy harvesting with multi-array thermoelectric generators," *IEEE Trans. Ind. Electron.*, vol. 61, no. 10, pp. 5345–5353, Oct. 2014.
- [39] S.-U. Shin *et al.*, "A 95.2% efficiency dual-path DC-DC step-up converter with continuous output current delivery and low voltage ripple," in *IEEE Int. Solid-State Circuits Conf. (ISSCC) Dig. Tech. Papers*, Feb. 2018, pp. 430–432.
- [40] C.-W. Liu, H.-H. Lee, P.-C. Liao, Y.-L. Chen, M.-J. Chung, and P.-H. Chen, "Dual-source energy-harvesting interface with cycle-by-cycle source tracking and adaptive peak-inductor-current control," *IEEE J. Solid-State Circuits*, vol. 53, no. 10, pp. 2741–2750, Oct. 2018.
- [41] S. Kiran, S. Cai, Y. Luo, S. Hoyos, and S. Palermo, "A 52-Gb/s ADC-based PAM-4 receiver with comparator-assisted 2-bit/stage SAR ADC and partially unrolled DFE in 65-nm CMOS," *IEEE J. Solid-State Circuits*, vol. 54, no. 3, pp. 659–671, Mar. 2019.
- [42] Z. Zeng *et al.*, "Design of sub-gigahertz reconfigurable RF energy harvester from –22 to 4 dBm with 99.8% peak MPPT power efficiency," *IEEE J. Solid-State Circuits*, vol. 54, no. 9, pp. 2601–2613, Sep. 2019.
- [43] Y. Li *et al.*, "Study of an electromagnetic ocean wave energy harvester driven by an efficient swing body toward the self-powered ocean buoy application," *IEEE Access*, vol. 7, pp. 129758–129769, 2019.



**Zizhen Zeng** (Student Member, IEEE) received the B.E. degree from Beihang University (BUAA), Beijing, China, in 2014, and the M.Sc. degree from The Hong Kong University of Science and Technology (HKUST), Hong Kong, in 2015. He is currently pursuing the Ph.D. degree in electrical engineering with the Analog and Mixed-Signal Center (AMSC), Texas A&M University, College Station, TX, USA.

From 2014 to 2016, he worked as a Research Assistant with The Hong Kong University of Science and Technology. In Summer 2018, he worked as a Design Intern with Silicon Labs, Austin, for CMOS Wi-Fi power amplifier design. His research interests include low power circuit design, energy harvesting technologies, and power management circuit for wireless and biomedical applications. He was a recipient of the Texas Instruments Excellence Fellowship from 2017 to 2018 and 2018 to 2019.



**Johan J. Estrada-López** (Member, IEEE) was born in Mérida, Mexico. He received the B.Sc. degree from the Mérida Institute of Technology, Mérida, in 2001, the M.Sc. degree from the Center of Advanced Research and Studies (CINVESTAV), Guadalajara, Mexico, in 2003, and the Ph.D. degree from the Analog and Mixed-Signal Center, Texas A&M University, College Station, TX, USA, in 2019, all in electrical engineering.

From 2011 to 2013, he worked with Vidatronic, Inc. In 2017, he was a Design Intern with the Power Delivery Group, Intel Corporation, Hillsboro, OR, USA. In 2019, he worked as a Post-Doctoral Researcher with the Analog and Mixed-Signal Center, Texas A&M University. He is currently a Professor of computer engineering with the Autonomous University of Yucatan, Mexico. His current research interests include CMOS mixed-signal and analog circuit design for energy harvesting and power management in mobile and wearable applications, embedded system design for wireless sensor networks, and the Internet of Things applications. He was a recipient of the National Council of Science and Technology (CONACYT) Scholarship from the Government of Mexico from 2014 to 2019, the TI Jack Kilby Excellence, and Silicon Labs Fellowship at Texas A&M University.



**Bo Wang** (Member, IEEE) received the B.Eng. degree (Hons.) in electrical engineering from Zhejiang University, Hangzhou, China, in 2010, and the M.Phil. and Ph.D. degrees in electronic and computer engineering from The Hong Kong University of Science and Technology (HKUST), Hong Kong, in 2012 and 2015, respectively.

In 2015, he joined HKUST as a Post-Doctoral Researcher and led the HKUST-MIT Consortium Project on wireless sensing node design for smart green building applications. In 2016, he was with the Massachusetts Institute of Technology for a project on low power data converter design. In 2017, he joined Hamad Bin Khalifa University, Qatar Foundation, as a Founding Faculty, where he is currently an Assistant Professor with the Division of Information and Computing Technology, College of Science and Engineering. His research interests include the design of energy-efficient analog/mixed-signal circuits, sensor/sensor interface, and heterogeneous integrated systems for *in vitro/vivo* healthcare. He serves as a Technical Committee Member of the IEEE CAS Committee on sensory systems. He was a recipient of the IEEE ASP-DAC Best Design Award in 2016.



**Edgar Sánchez-Sinencio** (Life Fellow, IEEE) was born in Mexico City, Mexico. He received the Professional degree in communications and electronic engineering from the National Polytechnic Institute of Mexico, Mexico City, in 1966, the M.S.E.E. degree from Stanford University, Stanford, CA, USA, in 1970, the Ph.D. degree from the University of Illinois at Urbana-Champaign, Champaign, IL, USA, in 1973, and the Honoris Causa Doctorate (Hons.) degree in microelectronic circuit-design contributions from the National Institute for Astrophysics, Optics and Electronics, Mexico, in November 1995.

He was the University Distinguished Professor, the Texas Instruments Jack Kilby Chair Professor, and the Director with the Analog and Mixed-Signal Center, Texas A&M University, College Station, TX, USA. He has graduated 61 M.Sc. and 59 Ph.D. students. He was the coauthor of six books on different topics, such as RF circuits, low-voltage low-power analog circuits, and neural networks. His current interests include the area of ultralow power analog circuits, RF circuits, harvesting techniques, power management, and medical electronics circuit design.

Dr. Sánchez-Sinencio was a member of the IEEE Solid-State Circuits Society Fellow Award Committee from 2002 to 2004 and a fellow of the Institution of Engineering and Technology, which is the largest multidisciplinary professional engineering institution in the world. He was a recipient of the Texas Senate Proclamation #373 for Outstanding Accomplishments in 1996, the IEEE Circuits and Systems Society Golden Jubilee Medal in 1999, and the prestigious IEEE Circuits and Systems Society 2008 Charles A. Desoer Technical Achievement Award. He was a co-recipient of the 1995 Guillemin-Cauer Award for his work on cellular networks and the 1997 Darlington Award for his work on high-frequency filters. He was the IEEE Circuits and Systems Society's Representative to the IEEE Solid-State Circuits Society from 2000 to 2002. He was the former IEEE Circuits and Systems Society's Vice President-Publications. He was the former Editor-in-Chief of the *IEEE TRANSACTIONS ON CIRCUITS AND SYSTEMS—II: EXPRESS BRIEFS*. He was a Guest Editor of the Analog Section of the *IEEE JOURNAL OF SOLID-STATE CIRCUITS* special issue of December 2016. He was a Co-Guest Editor of the *Circuits and Systems for the Internet of Things* Special Issue on from sensing to sensemaking published in September 2017. He was a former Distinguished Lecturer of the IEEE Circuit and Systems Society from 2012 to 2013.